catalysts

MDPI

Article

Optimizing Citrate Combustion Synthesis of A-Site-Deficient La,Mn-Based Perovskites: Application for Catalytic CH_4 Combustion in Stoichiometric Conditions

Andrea Osti *, Lorenzo Rizzato, Jonathan Cavazzani and Antonella Glisenti *

Department of Chemical Sciences, University of Padova, Via F. Marzolo, 1, 35131 Padova, Italy; lorenzo.rizzato.1@phd.unipd.it (L.R.); jonathan.cavazzani@phd.unipd.it (J.C.)
* Correspondence: andrea.osti.1@phd.unipd.it (A.O.); antonella.glisenti@unipd.it (A.G.)

Abstract: $LaMnO_3$-based perovskites are widely recognized as promising catalysts for several oxidation reactions, but the final physicochemical and catalytic properties can be greatly influenced by the adopted synthesis procedure. In this work, a series of A-site-deficient perovskites of composition $La_{0.8}MnO_3$ and $La_{0.8}Mn_{0.9}B_{0.1}O_3$ (B = Ni, Cu) were prepared through the citrate combustion route with variations in two synthesis parameters: a citric acid/metal cations molar ratio (CA/M) of either 1.1 or 1.5 and either acidic (given by HNO_3 + citric acid) or neutral (after NH_3 addition) pH of the precursor solution. The obtained samples were characterized by XRD, H_2-TPR, O_2-TPD, N_2 physisorption, SEM-EDX and XPS. Acidic pH coupled with a CA/M ratio of 1.1 clearly emerged superior among all the other combinations of the two parameters, resulting in smaller crystallite size, higher surface area and porosity, enhanced Mn^{4+} reducibility and the ability to release oxygen species; these features were even further improved by B-site substitution with 10 mol% Ni and Cu cations. The synthesized catalysts were tested in CH_4 oxidation to CO_2 under stoichiometric O_2, confirming the great superiority of samples prepared in acidic pH with a CA/M ratio of 1.1. Ni and Cu doping had a beneficial effect on catalytic activity, which, however, was more evident for less optimized perovskites (acidic pH and CA/M ratio of 1.5), without significance differences among the two dopants.

Keywords: $La_{0.8}MnO_3$ perovskite; Ni and Cu doping; citrate combustion synthesis; heterogeneous catalysis; CH_4 combustion

Citation: Osti, A.; Rizzato, L.; Cavazzani, J.; Glisenti, A. Optimizing Citrate Combustion Synthesis of A-Site-Deficient La,Mn-Based Perovskites: Application for Catalytic CH_4 Combustion in Stoichiometric Conditions. *Catalysts* **2023**, *13*, 1177. https://doi.org/10.3390/catal13081177

Academic Editors: Leonarda Liotta, Narendra Kumar and Konstantin Ivanov Hadjiivanov

Received: 23 June 2023
Revised: 25 July 2023
Accepted: 29 July 2023
Published: 1 August 2023

1. Introduction

Perovskite oxides with the general formula ABO_3 have attracted much attention in the last decades as catalysts in many reactions because of their stable crystal structure, hydrothermal stability, redox activity, great composition tunability and defect engineering [1,2]. Among them, $LaMnO_3$-based perovskites have been widely studied as promising catalysts for several oxidation (to CO_2) reactions, of, e.g., CO, volatile organic compounds (VOCs) and hydrocarbons (HCs) [3–5]. Factors like exposed surface area, cation reducibility, the content of highly valent cations (e.g., Mn^{4+} compared to the main Mn^{3+}) and the presence of mobile surface and lattice oxygen species have been reported to be decisive in perovskites to improve their catalytic activity in oxidation reactions [6–11]. However, such physicochemical properties can be greatly influenced by the adopted synthesis protocol, which must be properly optimized. The citrate combustion (or citrate sol-gel) route [12] has been extensively employed for the preparation of high-purity and crystalline oxide powders at a relatively low calcination temperatures (e.g., 600–900 °C), benefiting from the ability of citrate anions to complex and homogenously disperse metal cations, with the formation of a gel, which is then ignited at a suitable temperature through an in situ redox reaction between citric acid (fuel) and nitrates (oxidizer) used as precursors. The composition of the obtained gel, its combustion rate and heat generated upon burning

depend on the fuel/oxidizer molar ratio, also affecting the final perovskite's textural properties. For instance, Taguchi et al. prepared $LaMnO_3$ with a citric acid/sum of metal cations (CA/M) molar ratio of between 0.016 and 1.07 (moles of citric acid from 0.0023 to 0.015 in the paper), showing that the crystallite size reached a minimum and the surface area a maximum at CA/M of about 0.5–0.6 (0.007 and 0.008 moles of citric acid), above which the combustion heat increased, negatively affecting the surface area [13]. Ghiasi et al. prepared $LaMnO_3$ with a citric acid/sum of nitrates ratio from 1.0 to 5.0 (corresponding to CA/M of 2.5 to 12.5), highlighting that the stoichiometric amount of citric acid (1.0 vs. nitrates, 2.5 vs. metal cations) was the best for lowering crystallite size and particle agglomeration, whereas too high an amount of citric acid degraded the perovskite structure because of excessive heat of combustion [14]. Sihaib et al. prepared $LaMnO_3$ with a CA/M ratio from 0.5 to 2.0, evidencing that intermediate CA/M values of 1.2 to 1.5 led to the lowest crystallite size, enhanced surface area, greater Mn^{4+} reducibility, the highest Mn/La surface ratio and, accordingly, better catalytic activity in toluene and propene oxidation [15]. When NH_3 was added to the $LaMnO_3$ precursor solution to neutralize the pH, as in the work of Li et al. with citric acid/nitrates ratio ranging from 0.5 to 3.0 (corresponding to CA/M of 1.25 to 7.5), the lowest particle size was obtained with a lower amount of citric acid (0.5 and 1.0 vs. nitrates, 1.25 and 2.5 vs. metal cations), although the phase purity was the maximum at a citric acid/nitrate ratio of 1.5 (CA/M = 3.75) [16]. These works point out the necessity of finding the right fuel/oxidizer molar ratio, which can vary depending on the other synthesis parameters (like precursor solution pH and calcination temperature). Furthermore, charge imbalances at the A-site, achieved by aliovalent doping (e.g., Sr^{2+} partially replacing La^{3+}) or by means of A-site cation deficiency, are known to increase the number of oxygen vacancies, which is useful for improving reactant adsorption and enhancing oxygen mobility [1,5,17]. A-site deficiency can also be desirable to counteract the usually observed La surface enrichment (non-redox active) and to increase the B-site cation oxidation state and reducibility [9,18,19]. Accordingly, $LaMn_{1.2}O_{3+\delta}$ (or $La_{0.83}MnO_3$) was found to be more active than stoichiometric $LaMnO_3$ towards CO and C_3H_8 oxidation [19]. A partial replacement of Mn at the B-site by either Ni or Cu cations was also shown to improve HCs' oxidation capability, thanks to improved surface area, reducibility and surface oxygen mobility [20,21]

Based on the above considerations, in the present work, a series of A-site-deficient $La_{0.8}MnO_3$ perovskites were synthesized by the citrate combustion route, with variations in terms of two synthesis parameters: a CA/M ratio of either 1.1 or 1.5 and either an acidic (given by HNO_3 and citric acid) or neutral (upon NH_3 addition) pH of the precursor solution. B-site doping with Ni and Cu cations was performed as well, preparing perovskites with the composition $La_{0.8}Mn_{0.9}Ni_{0.1}O_3$ and $La_{0.8}Mn_{0.9}Cu_{0.1}O_3$. The precursor gel decomposition process was analyzed by TGA, and the calcined samples were deeply characterized by XRD, N_2 physisorption, SEM-EDX, XPS, H_2-TPR and O_2-TPD techniques. The influence of the synthesis parameters (pH, CA/M ratio) and of B-site doping on physicochemical properties and on catalytic activity towards CH_4 combustion with stoichiometric O_2 was evaluated.

2. Results and Discussion

2.1. Physicochemical Characterizations

2.1.1. Structural and Morphological Features

A list of the eight prepared perovskites and their synthesis conditions are reported in Table 1. The subscript 'H^+' is used to refer to samples synthesized in acidic precursor solution before the gel formation, as determined by HNO_3 and citric acid, whereas the subscript 'NH_3' indicates samples prepared through pH neutralization by NH_3 addition before the gel formation (see Section 3.1 Synthesis protocol). The molar ratio citric acid/sum of metal cations (either 1.1 or 1.5) is indicated by the notation 'CA1.1' and 'CA1.5'. Let us note that the variation in the amount of citric acid (CA1.1 or CA1.5) in the acidic precursor solution did not substantially change the final pH, which was always <1 and probably even

negative. This was primarily governed by the strong acid HNO_3. The ignition temperature was varied depending on whether or not NH_3 was introduced into the precursor solution, as further explained in Section 2.1.2. The chosen calcination temperature (750 °C) was a compromise between the necessity of approaching the conditions employed in the catalytic test (up to 800 °C) and the need to avoid excessive sintering induced by high temperatures.

Table 1. Prepared samples and synthesis conditions. CA/M* = citric acid/metal cations molar ratio.

Sample	CA/M* Molar Ratio	pH of Synthesis	Ignition T (°C)	Calcination T (°C)
$La_{0.8}MnO_3$-NH_3-CA1.1	1.1	7	350	750
$La_{0.8}MnO_3$-NH_3-CA1.5	1.5	7	350	750
$La_{0.8}MnO_3$-H^+-CA1.1	1.1	<1	200–230	750
$La_{0.8}MnO_3$-H^+-CA1.5	1.5	<1	200–230	750
$La_{0.8}Mn_{0.9}Ni_{0.1}O_3$-$H^+$-CA1.1	1.1	<1	200–230	750
$La_{0.88}Mn_{0.9}Ni_{0.1}O_3$-$H^+$-CA1.5	1.5	<1	200–230	750
$La_{0.88}Mn_{0.9}Cu_{0.1}O_3$-$H^+$-CA1.1	1.1	<1	200–230	750
$La_{0.88}Mn_{0.9}Cu_{0.1}O_3$-$H^+$-CA1.5	1.5	<1	200–230	750

XRD patterns of the synthesized perovskites are reported in Figure 1. For all of them, the recorded diffractograms match with the hexagonal perovskite phase $La_{0.887}MnO_3$ (space group R-3c:H, COD reference 1531294), with the characteristic reflection splitting of hexagonal $LaMnO_3$-type structures (see Figure S1). Additionally, for all $La_{0.8}MnO_3$ samples except H^+-CA1.1, weak reflections at 2θ = 36.1° and 2θ = 59.9° are probably ascribed to the presence of small Mn_3O_4 impurities, making these compositions less A-site-deficient than expected by stoichiometry. In the case of Ni-doped samples, no evident secondary phases emerged from the XRD patterns, which suggests the complete Ni^{2+} (or possibly Ni^{3+}) incorporation inside the perovskite lattice at 10 mol% doping. Instead, Cu-doped samples seem to display a weak reflection at 2θ = 36.0° ascribed to the $CuMn_2O_4$ spinel phase. Thus, Cu^{2+} cations are not completely incorporated in the perovskite framework, probably because of a larger size difference with respect to Mn^{3+} main cations than in the case of Ni doping (0.72 Å Mn^{3+}, 0.87 Å Cu^{2+}, 0.83 Å Ni^{2+}, 0.74 Å Ni^{3+} [22]). It is interesting to note that samples prepared in acidic pH, and especially those with CA1.1, exhibit broader reflections and a less defined splitting, suggesting the presence of smaller crystallites with respect to samples prepared with NH_3 neutralization. Indeed, average crystallite size values reported in Table 2, calculated by means of the Williamson–Hall method, support this observation: the grain size tends to decrease for acidic pH synthesis and especially when there is less citric acid (CA1.1 samples), and the size tends to be even smaller after Ni and Cu doping compared to undoped $La_{0.8}MnO_3$ prepared with the same synthesis protocol, as already found in the literature [20,21]. The lowest crystallite size, 23 nm, was obtained for $La_{0.8}Mn_{0.9}Ni_{0.1}O_3$-$H^+$-CA1.1; the highest, 82 nm, for $La_{0.8}MnO_3$-NH_3-CA1.5. For the sake of comparison, Ghiasi et al. obtained $LaMnO_3$ with an average grain size ranging from 30 to 70 nm depending on the amount of citric acid and the calcination temperature [14]; Gholizadeh prepared $LaMnO_3$ calcined at 900 °C with an average size of 53 nm [23]; and Frozandeh-Mehr et al. obtained a crystallite size of just 14 nm for $LaMnO_3$ with a low calcination temperature of 600 °C [24]. Thus, crystallite sizes obtained in the present work are in reasonable agreement with those reported in literature for similar compositions and synthesis methods.

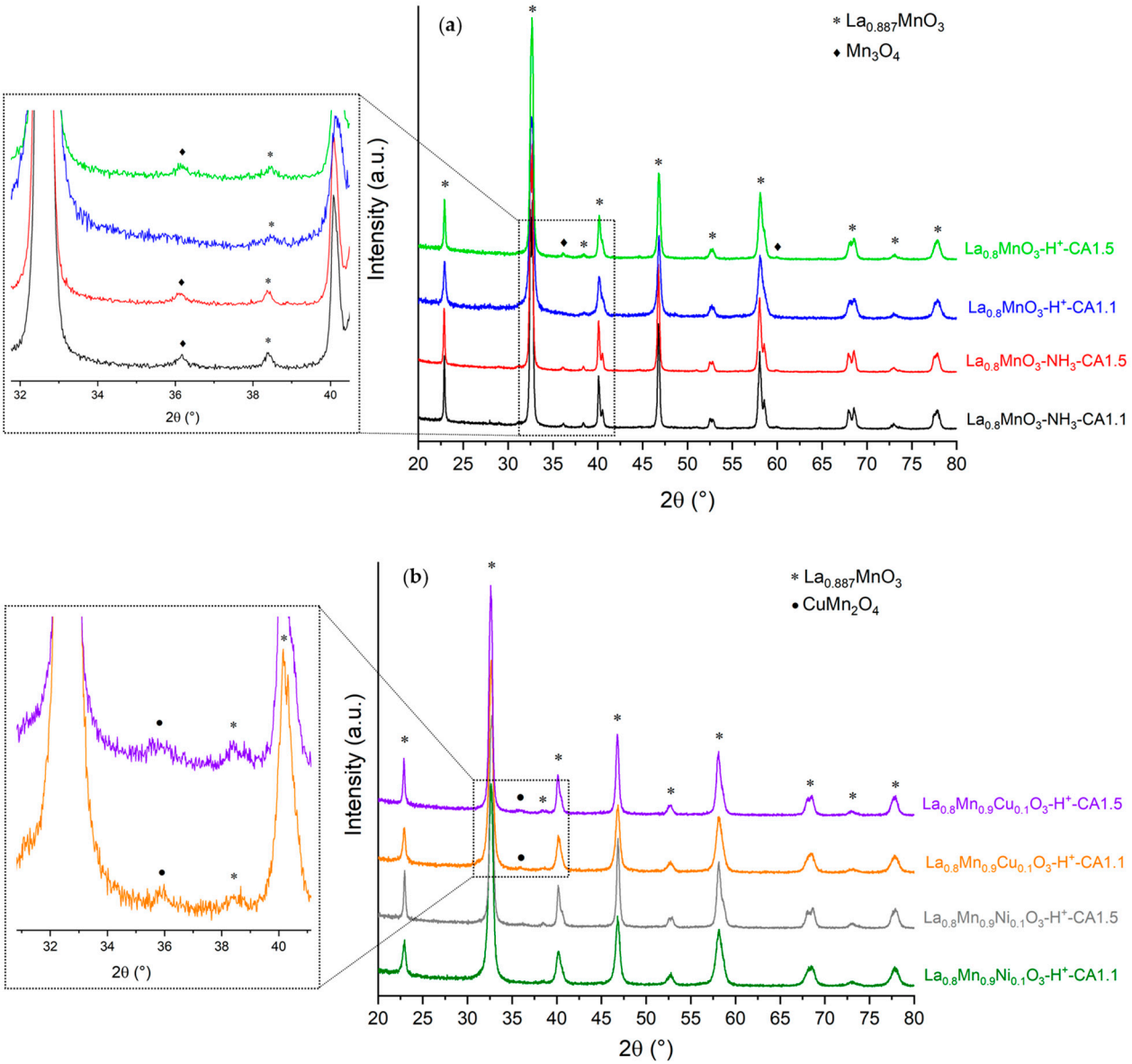

Figure 1. XRD patterns of (**a**) $La_{0.8}MnO_3$ samples, with zoom highlighting the presence of a weak Mn_3O_4 reflection at 2θ = 36.1°; (**b**) Ni- and Cu-doped samples, with zoom highlighting the presence of a weak $CuMn_2O_4$ reflection at 2θ = 36.0° on samples containing Cu.

Table 2. Specific surface area (SSA), total pore volume and average crystallite size (d_{XRD}) of the eight prepared perovskites.

Sample	SSA (m^2/g) [1]	Pore Vol. (cm^3/g) [2]	d_{XRD} (nm) [3]
$La_{0.8}MnO_3$-NH_3-CA1.1	4.9	0.013	69.3
$La_{0.8}MnO_3$-NH_3-CA1.5	4.0	0.0070	81.5
$La_{0.8}MnO_3$-H^+-CA1.1	25.0	0.081	33.1
$La_{0.8}MnO_3$-H^+-CA1.5	4.2	0.016	64.8
$La_{0.8}Mn_{0.9}Ni_{0.1}O_3$-$H^+$-CA1.1	43.9	0.152	22.7
$La_{0.88}Mn_{0.9}Ni_{0.1}O_3$-$H^+$-CA1.5	7.6	0.039	46.8
$La_{0.88}Mn_{0.9}Cu_{0.1}O_3$-$H^+$-CA1.1	37.1	0.145	33.0
$La_{0.88}Mn_{0.9}Cu_{0.1}O_3$-$H^+$-CA1.5	11.7	0.037	45.1

[1] Determined by BET method; [2] determined by BJH method; [3] determined by Williamson–Hall method, with K = 0.90 and λ = 0.154 nm.

In Figure 2, N_2 adsorption–desorption isotherms of the eight samples are reported, and the corresponding pore size distributions calculated from the desorption branches are shown in Figure S2. Specific surface area (SSA) and total pore volume, determined by BET and BJH methods, respectively, are listed in Table 2. Adsorption isotherms are similar to type III, with no evident "point B", indicating a weak N_2-adsorbent interaction; however, a type H3 hysteresis also appears, suggesting the presence of macro/mesopores probably formed by loose aggregates of particles [25]. Despite the similar shape of isotherms and hysteresis loops regardless of the synthesis protocol, SSA and pore volume can vary to a relatively large extent. Among the four $La_{0.8}MnO_3$ samples, H^+-CA1.1 clearly emerges superior for its much higher SSA (25 m^2/g) and pore volume, both values being at least five times higher than those of the other three samples (4–5 m^2/g), which is related to a larger amount of mesopores, as shown in Figure S2. In general, the synthesis in acidic pH seems to be preferable compared to synthesis with NH_3 neutralization, although a higher amount of citric acid (1.5) reduces the benefits in terms of SSA and porosity. Similar values ranging from 5 to 26 m^2/g, depending on CA/M ratio, were obtained by Sihaib et al. for $LaMnO_3$ calcined at 750 °C [15], and Taguchi et al. obtained intermediate surface areas of 13–16 m^2/g (again as a function of the amount of CA) by calcining $LaMnO_3$ at 700 °C [13]. In some cases, La-deficient compositions were reported to have higher surface area values compared to stoichiometric ones. For instance, Chen et al. obtained a value of 23 m^2/g for $La_{0.9}MnO_3$, compared to 20 m^2/g for $LaMnO_3$, both calcined at 700 °C; a marked increase in surface area was obtained for $La_{0.7}FeO_3$ compared to $LaFeO_3$ as well [26]. The SSA values obtained in this work are therefore comparable to the findings in the literature. At a parity of CA, B-site doping with Ni or Cu cations is even more beneficial in enhancing SSA and mesoporosity compared to benchmark La and Mn perovskites, pushing SSA values close to or even higher than 40 m^2/g in the case of less CA (1.1), whereas the enhancement is less marked with CA of 1.5 (SSA of 7–11 m^2/g). All these observations correlate well with the crystallite size determined from XRD patterns: a decrease in grain size, especially for H^+-CA1.1 samples, is accompanied by a marked increase in surface area values and pore volume. Increases in SSA upon Ni or Cu doping were observed in the literature as well, e.g., 26 m^2/g for $LaMn_{0.9}Ni_{0.1}O_3$ compared to 20 m^2/g for $LaMnO_3$, both calcined at 750 °C [20], and 15 m^2/g for $LaMnCu_{0.1}O_3$ compared to 8 m^2/g for $LaMnO_3$, calcined at 700 °C [21]. The SSA values of 44 and 37 m^2/g obtained in this work for $La_{0.8}Mn_{0.9}Ni_{0.1}O_3$-$H^+$-CA1.1 and $La_{0.8}Mn_{0.9}Cu_{0.1}O_3$-$H^+$-CA1.1, respectively, are therefore even higher than those in many works in the literature.

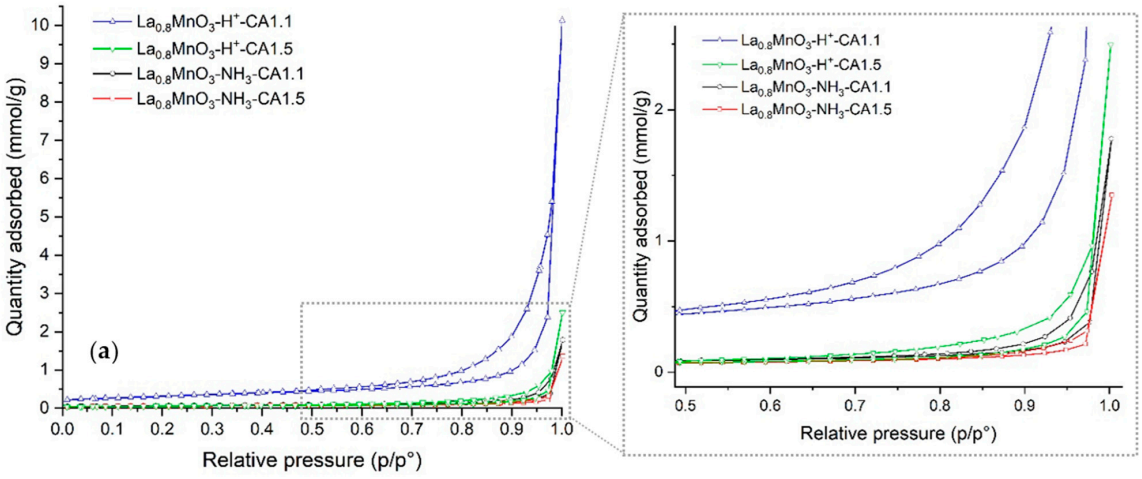

Figure 2. *Cont.*

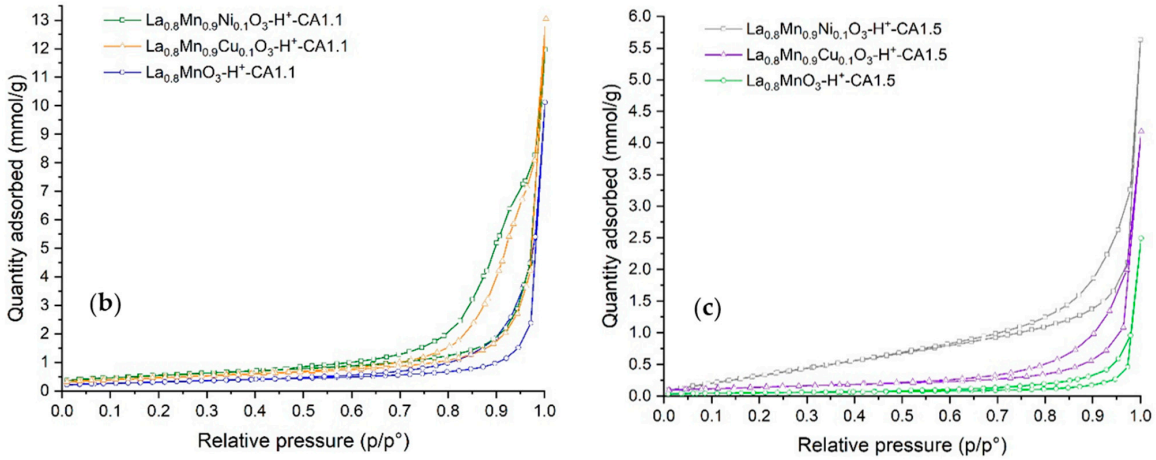

Figure 2. N_2 adsorption isotherm of the prepared catalysts: (**a**) the four $La_{0.8}MnO_3$ samples, with zoom on the high-pressure range of the low SSA samples; (**b**) Ni- and Cu-doped samples with CA1.1, compared to $La_{0.8}MnO_3$-H^+-CA1.1; (**c**) Ni- and Cu-doped samples with CA1.5, compared to $La_{0.8}MnO_3$-H^+-CA1.5.

Representative SEM micrographs of the eight prepared perovskites are shown in Figures 3 and S3. The morphology of NH_3 samples (Figures 3a and S3a) appears to be composed of particles with a size distribution from tens to hundreds of nm, which leave pores of variable dimension upon aggregation. In the case of H^+-CA1.1 samples (Figures 3b,c and S3c), individual grains are not clearly discernible, in agreement with their lower size calculated from XRD patterns, and many small pores in the meso-range are evident, especially for B-site-doped perovskites (Figures 3c and S3c), in agreement with N_2 physisorption results. H^+-CA1.5 samples (Figures 3d and S3b,d) have somewhat intermediate characteristics, with a more compact morphology compared to H^+-CA1.1 samples, as evidenced by the presence of several-µm-wide plate-like aggregates (Figure S3b,d) and of discernible grains (Figures 3d and S3b), although a certain mesoporosity can still be appreciated, especially for Ni- and Cu-doped samples (Figures 3d and S3d). This is again in agreement with both XRD and N_2 physisorption results (e.g., intermediate SSA values and pore volume).

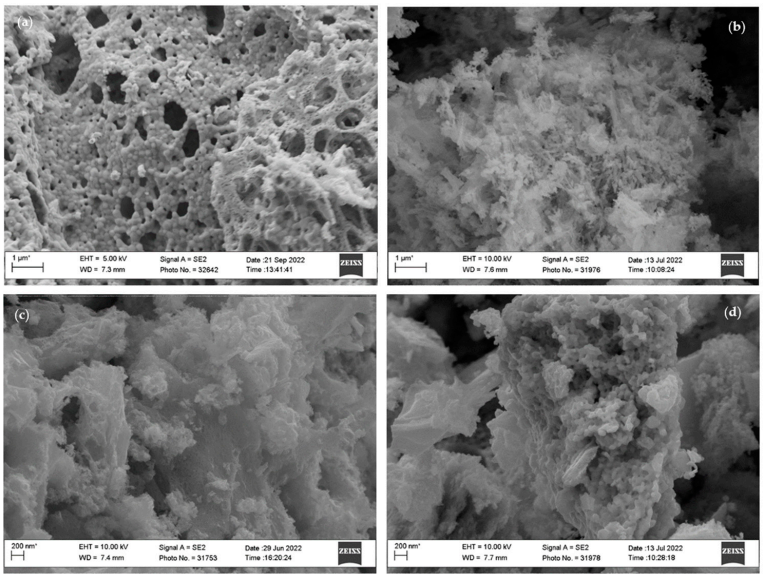

Figure 3. SEM micrographs of (**a**) $La_{0.8}MnO_3$-NH_3-CA1.1; (**b**) $La_{0.8}MnO_3$-H^+-CA1.1; (**c**) $La_{0.8}Mn_{0.9}Ni_{0.1}O_3$-$H^+$-CA1.1; (**d**) $La_{0.8}Mn_{0.9}Ni_{0.1}O_3$-$H^+$-CA1.5. Images (**a**,**b**) are taken at 25,000× magnification, images (**c**,**d**) at 50,000× magnification.

2.1.2. Precursor Decomposition

Since the calcination temperature was kept equal for all catalysts, the differences in morphological properties at varying synthesis parameters, as evidenced by XRD, N_2 physisorption and SEM, are clearly dependent on how the exothermic reaction occurs between nitrate oxidizer and citrate fuel during the perovskite synthesis process. By empirical observation, we generally noted that gels of samples prepared in acidic pH required temperatures lower than 250 °C (sometimes just above 150 °C) to start decomposing, with the evolution of gases and a change in color from yellowish/greenish to dark brown, as if carbonized. On the other hand, gels obtained after the addition of NH_3 seemed to require a temperature above 250 °C for this process to occur, at first with the evolution of gases, then with a clearly visible flame, which was not observed in the former case, producing a grey/black ash-like solid. To try to better understand the process of gel decomposition, thermogravimetric analysis (TGA) was carried out on four selected gel precursors after being dried at 120 °C; the resulting weight loss and corresponding first derivative profiles as a function of temperature are reported in Figure 4. As a general trend, a small weight loss of 5–10 % at up to 120–150 °C is ascribed to the removal of residual water of hydration. The main weight loss of up to 50–70 %, occurring between about 150 and 350 °C, is due to the exothermic nitrate–citrate redox reaction, and further weak weight losses can be ascribed to the decomposition of residual carbonates up to ≈500 °C, as well as to the formation of the final perovskite structure with some oxygen release by further increasing the temperature [15]. The gel of the $La_{0.8}MnO_3$-H^+-CA1.1 sample shows a very sharp and one-step weight loss at 195 °C because of the nitrate–citrate reaction. For $La_{0.8}MnO_3$-NH_3-CA1.1, and especially for $La_{0.8}MnO_3$-H^+-CA1.5, such decomposition occurs in more than one step, extending through a wider temperature range (the former up to 270 °C, the latter up to 350 °C). The delayed onset of decomposition when increasing the CA/M ratio (with acidic pH syntheses) was observed in previous works as well [13,15,16], explained by the lower amount of nitrate oxidizer in proportion to the citrate fuel; the same authors reported that either the longer reaction time or the higher amount of citrate fuel resulted in higher local temperatures, which produced bigger crystallites and decreased the final surface area. The values of crystallite size and SSA that we obtained for $La_{0.8}MnO_3$-H^+-CA1.1 and $La_{0.8}MnO_3$-H^+-CA1.5 are in line with these observations. In the case of the $La_{0.8}MnO_3$-NH_3-CA1.1 sample, the TGA profile suggests that the decomposition of the gel's citrate matrix starts to occur before the expected temperature of 250 °C, although the sharpest weight loss occurs right after this temperature, which we postulate might be due to the exothermic decomposition of the NH_4NO_3 formed in situ [27], further triggering the complete decomposition of the gel. The highest total weight loss observed for this sample is likely due to the initial presence of NH_3. The higher crystallite size and poorer SSA values observed for NH_3 samples could be again due to the longer decomposition time as observed in TGA plots, or perhaps to the occurrence of the flame, which would be characterized by a very high local temperature, resulting in particle sintering and a decrease in SSA, with only a weak dependency on the CA/M ratio. Even for the gel of the $La_{0.8}Mn_{0.9}Ni_{0.1}O_3$-$H^+$-CA1.1 sample, a multiple-step weight loss extending to almost 350 °C was noticed, which is thus above the temperature at which the gel carbonization was observed (as it was for $La_{0.8}MnO_3$-H^+-CA1.5); in fact, such carbonization might occur with the first weight loss centered at ~190°C. The reason for the lower final crystallite size and higher SSA achieved through Ni doping (as well as Cu doping), compared to $La_{0.8}MnO_3$-H^+-CA1.1, seems not to be clarified by TGA alone; it could be more related to the perovskite unit cell distortion induced by dopant cations rather than to the gel decomposition process.

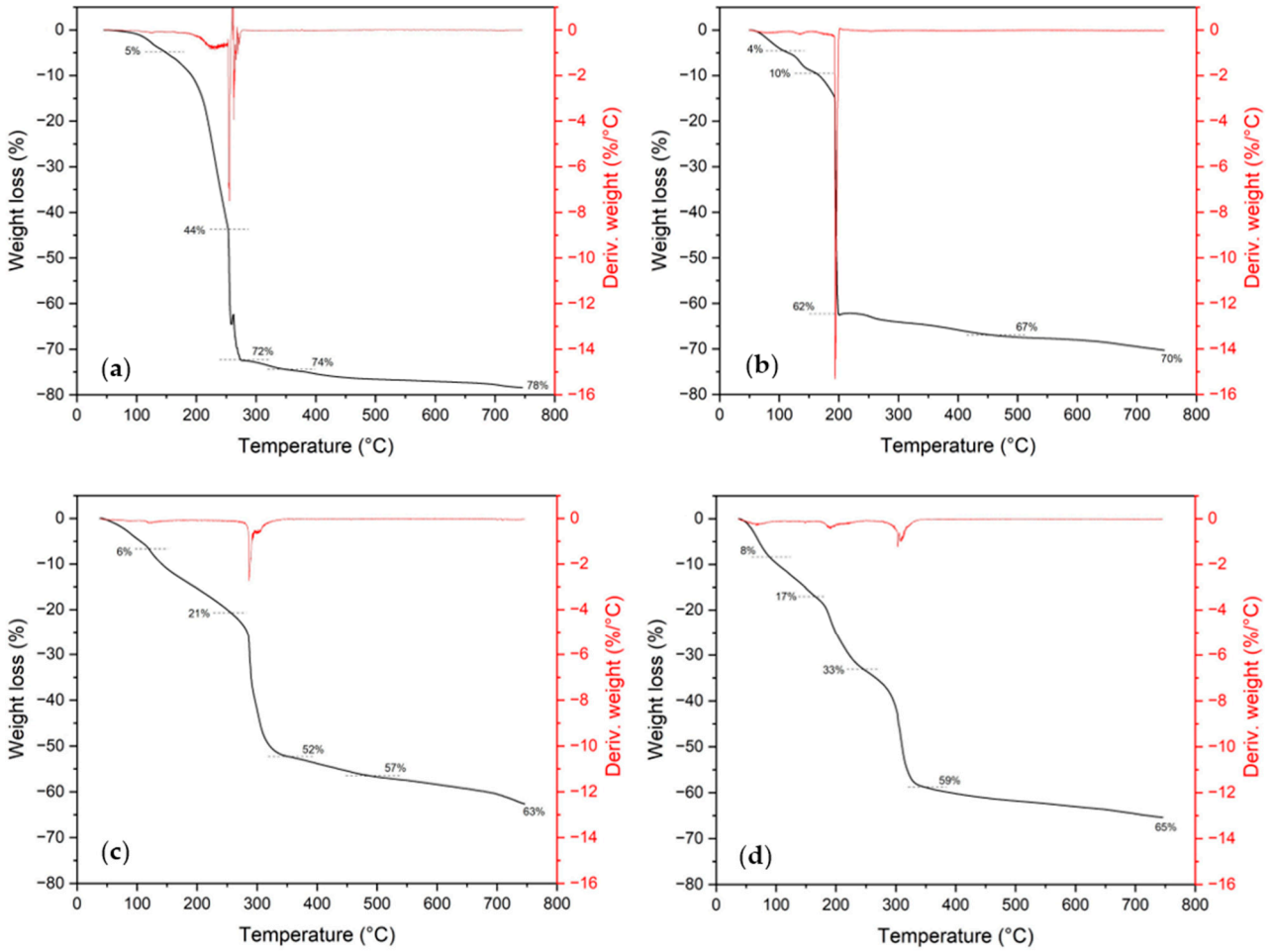

Figure 4. TGA weight loss as a function of temperature (black) and corresponding first derivative (red) of: (**a**) $La_{0.8}MnO_3$-NH_3-CA1.1; (**b**) $La_{0.8}MnO_3$-H^+-CA1.1; (**c**) $La_{0.8}MnO_3$-H^+-CA1.5; (**d**) $La_{0.8}Mn_{0.9}Ni_{0.1}O_3$-$H^+$-CA1.1.

2.1.3. Bulk and Surface Composition

The average perovskite composition until a depth of ~1 μm was explored by energy-dispersive X-ray analysis (EDX), and the average surface composition (depth of 5–10 nm) was explored by X-ray photoelectron spectroscopy (XPS). Element percentages are reported in Table S1 and Table 3, with and without considering the oxygen content, respectively, which is always excessive at the surface as well as in bulk, as usually occurs for perovskite oxides [28,29]. For all samples, all the expected elements (O, La, Mn, Ni/Cu, if any) were detected by both EDX and XPS, without evidence of a significant amount of impurities.

Table 3. Bulk (EDX) and surface (XPS) composition of the prepared perovskites, compared to the respective nominal amount according to sample stoichiometry.

Sample		La (at%) *	Mn (at%) *	Ni or Cu (at%) *
$La_{0.8}MnO_3$-NH_3-CA1.1	EDX	48.1	51.9	-
	XPS	45.0	55.0	-
	(nominal)	(44.5)	(55.5)	-
$La_{0.8}MnO_3$-NH_3-CA1.5	EDX	46.2	53.8	-
	XPS	42.9	57.1	-
	(nominal)	(44.5)	(55.5)	-

Table 3. *Cont.*

Sample		La (at%) *	Mn (at%) *	Ni or Cu (at%) *
$La_{0.8}MnO_3$-H^+-CA1.1	EDX	50.1	49.9	-
	XPS	41.7	58.3	-
	(nominal)	(44.5)	(55.5)	-
$La_{0.8}MnO_3$-H^+-CA1.5	EDX	46.5	53.5	-
	XPS	41.9	58.1	-
	(nominal)	(44.5)	(55.5)	-
$La_{0.8}Mn_{0.9}Ni_{0.1}O_3$-$H^+$-CA1.1	EDX	48.7	46.3	5.0
	XPS	37.9	60.1	2.0
	(nominal)	(44.5)	(50.0)	(5.5)
$La_{0.8}Mn_{0.9}Ni_{0.1}O_3$-$H^+$-CA1.5	EDX	48.3	45.7	6.0
	XPS	39.7	56.2	4.1
	(nominal)	(44.5)	(50.0)	(5.5)
$La_{0.8}Mn_{0.9}Cu_{0.1}O_3$-$H^+$-CA1.1	EDX	48.1	48.3	3.6
	XPS	37.2	51.5	11.3
	(nominal)	(44.5)	(50.0)	(5.5)
$La_{0.8}Mn_{0.9}Cu_{0.1}O_3$-$H^+$-CA1.5	EDX	48.2	45.7	6.1
	XPS	35.7	53.7	10.6
	(nominal)	(44.5)	(50.0)	(5.5)

* Metal percentage without considering the oxygen content.

In general, EDX reveals an enrichment in La and a deployment of Mn with respect to the nominal amounts, almost irrespective of the synthesis protocol, although this phenomenon seems more prominent in samples prepared in acidic pH. On the contrary, XPS reveals an opposite Mn enrichment at the expense of La, which is an effect of the A-site understoichiometry and could in principle be desirable for catalysis, with the surface being enriched with the redox active species (Mn^{n+}) [18]. Regarding Ni and Cu dopants, with EDX, there seems to be a slightly deficient amount with H^+-CA1.1 synthesis and a slightly excess amount in the case of H^+-CA1.5. At the surface, Ni is always deficient and Cu always in excess, likely confirming the complete Ni^{n+} incorporation inside the perovskite framework and the partial Cu^{2+} segregation as $CuMn_2O_4$ spinel, as revealed by XRD. Generally speaking, there are no evident correlations between synthesis parameters (CA/M ratio, pH) and the resulting surface and bulk composition.

2.1.4. Bulk Reducibility and Oxygen Mobility

Samples' reducibility was tested by H_2-TPR. The recorded profiles are reported in Figure 5, and reduction temperatures and quantification of H_2 consumption are listed in Table 4. Starting from the benchmark $La_{0.8}MnO_3$ composition (Figure 4a), two main reduction processes are discernible: $Mn^{4+} \rightarrow Mn^{3+}$ reduction in the lower temperature range (~150–550 °C), in parallel with the removal of the excessive lattice oxygen with respect to metal cations, and $Mn^{3+} \rightarrow Mn^{2+}$ reduction in the higher temperature range (~600–900 °C), leading to perovskite decomposition into single oxides/hydroxides (La_2O_3 or $La(OH)_3$ + MnO) [9,19]. Although the described reduction events are the same for all samples, peaks' characteristics (shape, area and position) are quite variable depending on the adopted synthesis protocol. In particular, the peaks tend to shift towards lower temperatures when decreasing the amount of CA (1.1) in the precursor solution and with acidic pH (H^+) versus neutral pH (NH_3), indicating a more ready reducibility. Indeed, $La_{0.8}MnO_3$-H^+-CA1.1 is by far the most reducible catalyst among the four, with the $Mn^{4+} \rightarrow Mn^{3+}$ reduction anticipated by at least 40 °C compared to the other three; in parallel, its low-temperature H_2 uptake is much enhanced (at the expense of the high-temperature uptake), indicating a greater lattice stabilization of Mn^{4+} at the expense of Mn^{3+}, whereas the three samples of H^+-CA1.5, NH_3-CA1.1 and NH_3-CA1.5 show approximately the same H_2 uptake in both T

ranges. These results can be well interpreted in terms of the lower crystallite size and much greater surface area and porosity of the H^+-CA1.1 samples [15,19], leading to easier adsorption and activation of H_2 during TPR experiments in comparison to the other three samples, which displayed a very similar surface area and a weak Mn_3O_4 phase segregation, likely decreasing the amount of Mn^{4+} in the perovskite lattice. Furthermore, the low-temperature shoulder at 200–250 °C, evidently appearing only in H^+-CA1.1 samples, could be attributed to the reduction in highly reducible Mn^{4+} species, likely located at the abundant surface or pore sites of this sample; a similar result was obtained for nanocrystalline high-surface area CeO_2, which was shown to display an additional TPR peak at low temperatures compared to bulk low-surface area CeO_2 [30].

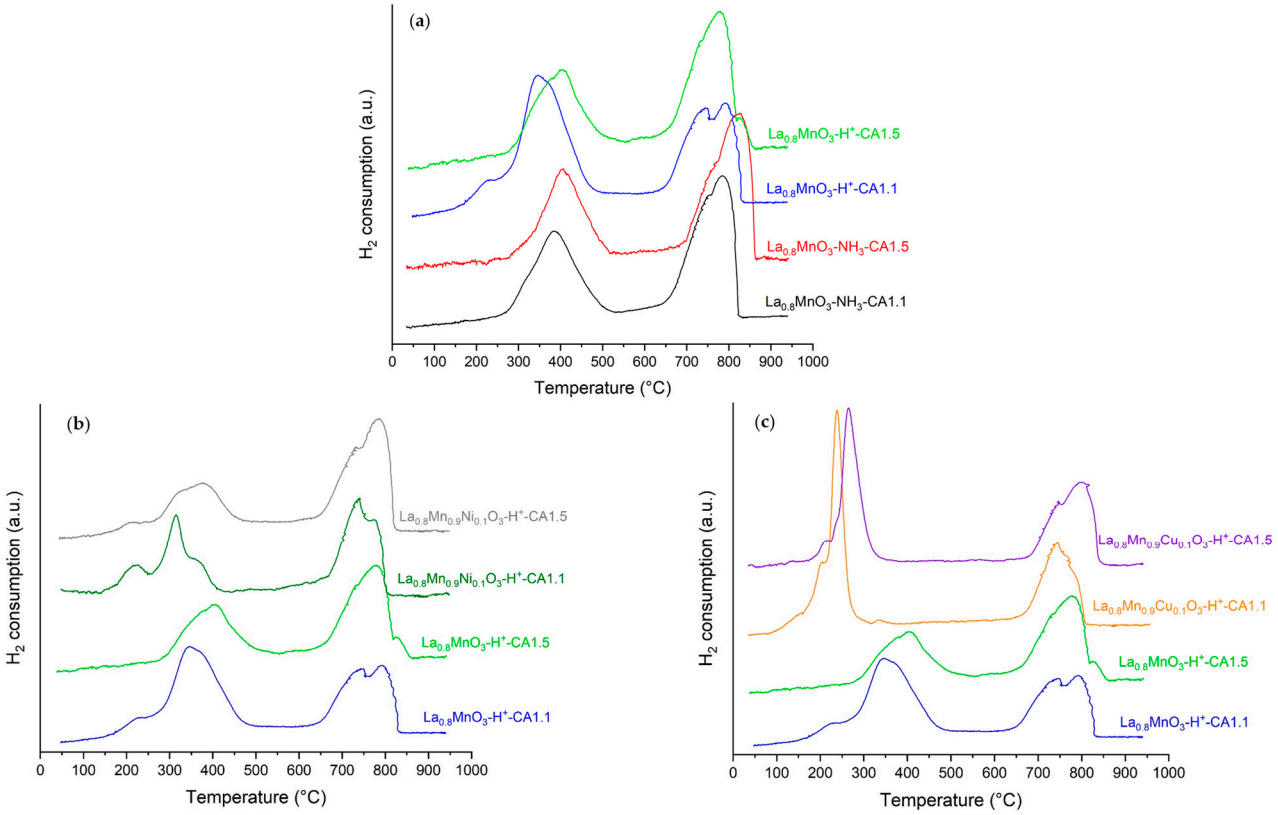

Figure 5. H_2-TPR profiles of: (**a**) the four $La_{0.8}MnO_3$ samples; (**b**) Ni-doped perovskites, compared to undoped ones prepared with the same protocol; (**c**) Cu-doped perovskites, compared to undoped ones prepared with the same protocol.

Table 4. Peak temperatures and quantitative analysis of H_2-TPR experiments.

Sample	Low Temperature Range [1]			High Temperature Range [2]		
	T_{max} (°C)	H_2 Uptake (mmol/g)	H/Mn + Cu	T_{max} (°C)	H_2 Uptake (mmol/g)	H/Mn + Ni
$La_{0.8}MnO_3$-NH_3-CA1.1	387	1.18	0.50	785	1.66	0.71
$La_{0.8}MnO_3$-NH_3-CA1.5	406	1.20	0.51	827	1.69	0.72
$La_{0.8}MnO_3$-H^+-CA1.1	346	1.85	0.79	794	1.32	0.56
$La_{0.8}MnO_3$-H^+-CA1.5	403	1.16	0.49	777	1.83	0.78
$La_{0.8}Mn_{0.9}Ni_{0.1}O_3$-$H^+$-CA1.1	315	1.35	0.58	740	1.73	0.74

Table 4. *Cont.*

Sample	Low Temperature Range [1]			High Temperature Range [2]		
	T_{max} (°C)	H_2 Uptake (mmol/g)	H/Mn + Cu	T_{max} (°C)	H_2 Uptake (mmol/g)	H/Mn + Ni
$La_{0.8}Mn_{0.9}Ni_{0.1}O_3$-$H^+$-CA1.5	378	1.02	0.44	785	1.96	0.84
$La_{0.8}Mn_{0.9}Cu_{0.1}O_3$-$H^+$-CA1.1	239	1.98	0.85	745	1.45	0.62
$La_{0.8}Mn_{0.9}Cu_{0.1}O_3$-$H^+$-CA1.5	265	1.59	0.68	793	1.68	0.72

[1] Corresponding to reduction steps $Mn^{4+} \rightarrow Mn^{3+}$ and $Cu^{2+} \rightarrow Cu^{+} \rightarrow Cu^{0}$; [2] corresponding to reduction steps $Mn^{3+} \rightarrow Mn^{2+}$ and $Ni^{2+} \rightarrow Ni^{0}$.

Considering, now, the Ni- and Cu-doped samples, the above written considerations about the influence of textural properties on reducibility are confirmed: at a parity of composition, H^+-CA1.1 samples are more reducible and display a greater lattice Mn^{4+} stabilization with respect to H^+-CA1.5 samples, thanks to lower crystallite size, abundant surface area and porosity, as obtained by XRD and N_2 physisorption. The effect of Cu B-site doping (Figure 3c) is quite evident: Cu^{2+} reduction to Cu^0 in two steps, with Cu^+ as an intermediary, appears on the TPR profile with two shoulders at very low temperatures (range 100–220 °C), confirmed by an increase in the total H_2 uptake at low temperatures as compared to un-doped perovskites. Furthermore, Mn^{4+} reduction is greatly anticipated (at more than 100 °C) compared to benchmark $La_{0.8}MnO_3$ and starts right after the complete reduction of Cu, thanks to the phenomenon of H_2 spillover from pre-formed Cu^0 particles to the perovskite support [21]. In contrast, Ni doping (Figure 3b) has a less marked effect: there are no evident peaks ascribed to Ni^{n+} reduction; based on previous literature with similar compositions [31], $Ni^{2+} \rightarrow Ni^0$ reduction might be located at around 600–650 °C, possibly hidden by the rising part in the Mn^{3+} reduction peak. In any case, Ni doping seems to render Mn^{4+} species slightly more reducible by anticipating their peak temperature of 20–30 °C compared to benchmark $La_{0.8}MnO_3$, although it is not clear whether this is an effect of Ni^{n+} cations themselves, or of the improved surface area and porosity arising from Ni^{n+} insertion in the lattice, as could be inferred by the enhancement of the low-temperature shoulder previously ascribed to highly reducible Mn^{4+} species located at surface/pore sites. Despite such improvement in Mn^{4+} reducibility, the total H_2 uptake in the low T region decreases, and that in the high T region increases upon Ni substitution, suggesting the presence of a greater amount of Mn^{3+} in the lattice at the expense of Mn^{4+}, as found elsewhere in the literature [32].

Apart from cation reducibility, oxygen mobility was further investigated by O_2-TPD on five selected samples. The O_2 desorption profiles are shown in Figure 6, and the calculation of evolved O_2 amounts at low and high temperatures is reported in Table 5. Let us note that the latter calculation cannot be considered very accurate because of the uncomplete desorption process at the maximum tested temperature of 900 °C, but it has been added for the sake of comparison among the different catalysts. Below 500 °C, the release of weakly bound surface oxygen species (α_1-O_2), likely chemisorbed on oxygen vacancies, can be detected; at intermediate temperatures of approximately 550 to 700 °C, lattice oxygen still coming from the surface or near the surface (α_2-O_2) is desorbed; finally, above 700 °C, the release of bulk lattice oxygen (β-O_2) can be appreciated [3], even occurring in more than one step [20]. Notably, H^+-CA1.1 samples display the highest amount of α_1-O_2 desorption, especially the Ni-doped sample, in agreement with their easy reducibility at low temperatures and superior surface area values. $La_{0.8}MnO_3$-H^+-CA1.1 has the most prominent α_2- and β-O_2 release as well, whereas these decrease upon Ni doping; this suggests that the release of bulk lattice oxygen is accompanied by bulk $Mn^{4+} \rightarrow Mn^{3+}$ reduction, whose H_2-TPR peak was less marked on $La_{0.8}Mn_{0.9}Ni_{0.1}O_3$ compared to $La_{0.8}MnO_3$. $La_{0.8}MnO_3$-NH_3-CA1.1 and $La_{0.8}MnO_3$-H^+-CA1.5 samples do not show an evident α_1-O_2 peak; it is likely very weak and hidden by experimental noise due to low surface area and delayed Mn^{4+} reducibility compared to H^+-CA1.1 samples, whereas $La_{0.8}Mn_{0.9}Cu_{0.1}O_3$-$H^+$-CA1.5

samples display a higher amount of oxygen desorption in the whole range compared to undoped $La_{0.8}MnO_3$-H^+-CA1.5, thanks to the somewhat improved surface area and Mn^{4+} reducibility arising from B-site doping.

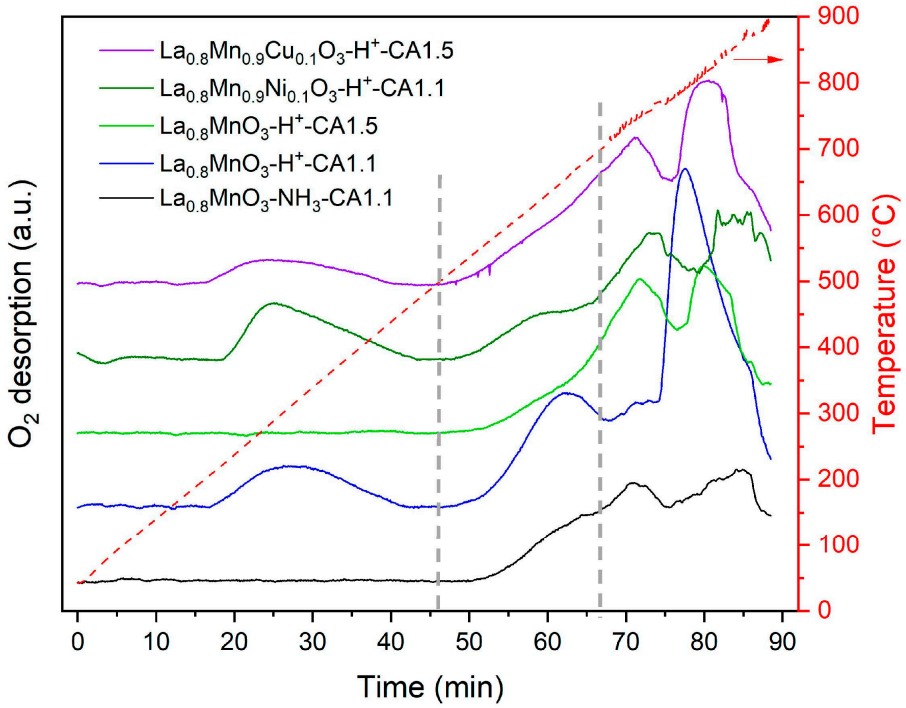

Figure 6. O_2-TPD profiles of five selected perovskites. Grey dotted vertical lines, at about 500 °C and 700 °C, roughly separate the three O_2 desorption stages: α_1, α_2 and β, in order of increasing T.

Table 5. Quantitative analysis of O_2-TPD experiments.

Sample	O_2 Desorption (μmol/g)	
	Low T Range (<500 °C)	High T Range (>500 °C)
$La_{0.8}MnO_3$-NH_3-CA1.1	-	86
$La_{0.8}MnO_3$-H^+-CA1.1	28	296
$La_{0.8}MnO_3$-H^+-CA1.5	-	149
$La_{0.8}Mn_{0.9}Ni_{0.1}O_3$-$H^+$-CA1.1	46	145
$La_{0.8}Mn_{0.9}Cu_{0.1}O_3$-$H^+$-CA1.5	8.3	208

2.2. Catalytic Activity

The prepared A-site-deficient perovskites were tested as catalysts for the complete combustion of CH_4 to CO_2 under a stoichiometric amount of O_2, as a model reaction occurring on methane-fed vehicles' three-way catalytic converters (TWC) [33]. No pre-treatment of the catalyst was performed, but further tests with a pre-reduction under diluted H_2 before exposure to the reaction mixture are currently ongoing, possibly modifying the final catalytic performances. CH_4 light-off conversion curves are reported in Figure 7, and the values of T_x (temperature necessary to achieve a certain value x of CH_4 conversion) and the reaction rates at 600 °C are listed in Table 6.

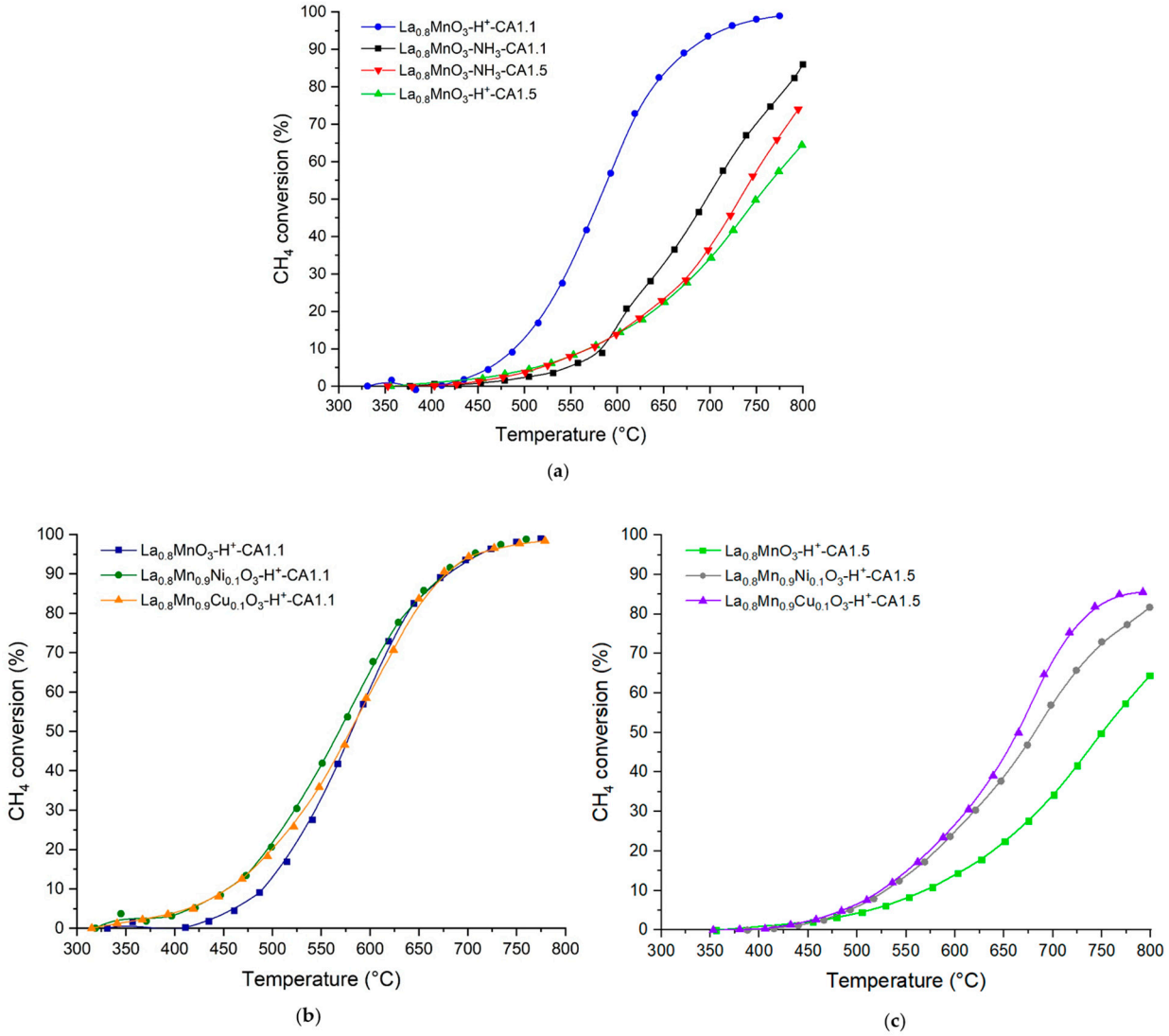

Figure 7. CH_4 conversion light-off curves of: (**a**) the four $La_{0.8}MnO_3$ samples; (**b**) Ni- and Cu-doped samples with CA1.1, compared to $La_{0.8}MnO_3$-H^+-CA1.1; (**c**) Ni- and Cu-doped samples with CA1.5, compared to $La_{0.8}MnO_3$-H^+-CA1.5.

Table 6. CH_4 oxidation performance of the prepared catalysts: temperature of 10%, 50% and 80% CH_4 conversion, specific and intrinsic reaction rates at 600 °C.

Sample	T_{10} (°C)	T_{50} (°C)	T_{80} (°C)	$r_{specific}$ (mol/s/g)	$r_{intrinsic}$ (mol/s/m^2)
$La_{0.8}MnO_3$-NH_3-CA1.1	583	696	783	3.7×10^{-6}	7.5×10^{-7}
$La_{0.8}MnO_3$-NH_3-CA1.5	570	732	>800	3.5×10^{-6}	8.8×10^{-7}
$La_{0.8}MnO_3$-H^+-CA1.1	489	581	639	9.9×10^{-6}	4.0×10^{-7}
$La_{0.8}MnO_3$-H^+-CA1.5	569	750	>800	3.6×10^{-6}	8.7×10^{-7}
$La_{0.8}Mn_{0.9}Ni_{0.1}O_3$-$H^+$-CA1.1	455	568	637	1.0×10^{-5}	2.3×10^{-7}
$La_{0.88}Mn_{0.9}Ni_{0.1}O_3$-$H^+$-CA1.5	528	681	790	5.6×10^{-6}	7.4×10^{-7}
$La_{0.88}Mn_{0.9}Cu_{0.1}O_3$-$H^+$-CA1.1	455	580	644	1.0×10^{-5}	2.7×10^{-7}
$La_{0.88}Mn_{0.9}Cu_{0.1}O_3$-$H^+$-CA1.5	524	664	736	6.2×10^{-6}	5.3×10^{-7}

Before examining the activity of the different samples, it is useful to introduce the mechanism of CH_4 (and other HCs) combustion on perovskite oxides. The reaction is reported to follow the Mars–Van Krevelen (MvK) mechanism [34], in which oxygen species on the perovskite surface are the primary active species for the reactant activation and

complete oxidation to CO_2; the release of oxygen species induces the formation of oxygen vacancies (V_O) on the catalyst surface and the parallel reduction in B-site cations (in this case, $Mn^{4+} \rightarrow Mn^{3+}$); finally, gas-phase oxygen is dissociatively adsorbed on the perovskite surface, thus replenishing V_O and reoxidizing the reduced cations. However, such oxygen species can be different depending on the temperature range: at low temperatures, the mechanism is suprafacial, meaning that the reaction involves weakly bound oxygen species directly adsorbed on the catalyst surface, particularly on V_O, which is easily exchangeable with gaseous O_2; at high temperatures, the diffusion of lattice oxygen becomes thermally activated, and thus lattice oxygen species present in the sub-surface layers can migrate to the reaction sites to oxidize the reactant and/or replenish the generated V_O. Here, the mechanism is referred to as intrafacial [6–8,19,35]. Therefore, in addition to the amount of exposed surface active sites, other important factors for catalytic activity are the content of highly valent Mn^{4+} ions and their ease of reducibility, in connection with a facile release of weakly adsorbed oxygen species at low temperatures, and with a fast mobility of lattice oxygen at high temperatures.

All catalysts produce CO_2 with selectivity close to 100% as a product of CH_4 oxidation (a very low and hardly quantifiable amount of CO was detected in a few cases), since the stoichiometric amount of O_2 in the gaseous mixture and the ability of perovskites to release active oxygen in general prevent uncomplete combustion. Among undoped $La_{0.8}MnO_3$ compositions, the H^+-CA1.1 sample is by far the most active, having an anticipated T_{50} value of more than 100 °C compared to the other three samples; it is also the only sample that is able to achieve full CH_4 conversion at 800 °C. This is evidently an effect of the superior surface area, porosity, Mn^{4+} reducibility and surface and bulk oxygen mobility and is also possibly due to the absence of Mn_3O_4 segregated phases, as revealed by physicochemical characterizations. The other three samples, NH_3-CA1.1, NH_3-CA1.5 and H^+-CA1.5, have quite similar activities, since their physicochemical properties are not much different (e.g., SSA = 4–5 m^2/g for all), although the NH_3-CA1.1 sample seems to perform slightly better than the other two above 600 °C, possibly thanks to a slightly easier Mn^{4+} reducibility (T_{max} at TPR of 387 °C compared to 403–406 °C of H^+-CA1.5 and NH_3-CA1.5). The calculation of specific reaction rates (i.e., at parity of the catalyst weight) at 600 °C confirm the superiority of the H^+-CA1.1 sample and the similar performances of the other three samples. However, the trend in the intrinsic rate values (normalized by surface area and thus linked to the single active sites' activity) is not in agreement with a specific rate trend, with H^+-CA1.1 having the lowest intrinsic rate. This likely supports the thesis that specific surface area, implying a greater exposure of active sites, is one of the main factors in improving catalytic activity, since it also influences active Mn^{4+} ions' reducibility and the ability to release active oxygen species.

Concerning Cu- and Ni-doped perovskites, analogous considerations about the influence of different synthesis protocols on catalytic activities can be formulated. Samples prepared with a lower CA/M ratio (1.1 vs. 1.5) perform much better, thanks to more favorable morphological features and Mn^{4+} reducibility. H^+-CA1.5 samples are indeed not able to reach complete CH_4 conversion in the tested temperature range and have much greater T_{50} values (of at least 85 °C) compared to H^+-CA1.1 samples. The comparison with undoped $La_{0.8}MnO_3$ compositions reveals some activity gain upon Ni or Cu doping, which is more evident in the case of H^+-CA1.5 samples: the T_{50} values are 681 and 664 °C for $La_{0.8}Mn_{0.9}Ni_{0.1}O_3$ and $La_{0.8}Mn_{0.9}Cu_{0.1}O_3$, respectively (vs. 750 °C for undoped composition), with Cu doping performing slightly better than Ni doping in the higher temperature region. The better performances are always related to better surface area and porosity resulting from B-site doping, confirmed by the calculation of reaction rates at 600 °C: specific rates (per unit of mass) are greater for doped samples compared to undoped ones, and the reverse is true for intrinsic rates (per unit of exposed surface). O_2-TPD further proved that $La_{0.8}Mn_{0.9}Cu_{0.1}O_3$-$H^+$-CA1.5 can release a higher amount of active surface and bulk lattice oxygen species compared to $La_{0.8}MnO_3$-H^+-CA1.5. The activity enhancement achieved through B-site doping is instead almost negligible for H^+-CA1.1 samples, appearing only

at low temperatures and to a slight extent: T_{10} = 455 °C for both $La_{0.8}Mn_{0.9}Ni_{0.1}O_3$ and $La_{0.8}Mn_{0.9}Cu_{0.1}O_3$, with respect to 489 °C for $La_{0.8}MnO_3$, whereas T_{50} and T_{80} are very similar for the three samples. In this case, the improved surface area only brings benefits to the low-temperature activity by enhancing the amount of surface oxygen release, as shown by O_2-TPD, thus facilitating the suprafacial mechanism; conversely, the mobility of surface and lattice oxygen is not enhanced by B-site doping (at least by Ni doping), thus not accelerating the intrafacial mechanism. A temperature value of around 600 °C might be the threshold for the change in the CH_4 oxidation mechanism under the tested conditions (stoichiometric amount of O_2), roughly corresponding to the temperature needed to activate surface lattice oxygen (α_2-O_2) at TPD. Overall, the most active catalyst is $La_{0.8}Mn_{0.9}Ni_{0.1}O_3$-$H^+$-CA1.1, which is the catalyst with the highest specific surface area.

3. Materials and Methods

3.1. Synthesis Protocol

$La_{0.8}MnO_3$ perovskites were prepared according to the citrate combustion route. The selected amount of La_2O_3 (≥99.9% Sigma-Aldrich, Beijing, China) and $Mn(acetate)_2{\cdot}4H_2O$ (≥99% Sigma-Aldrich, Schnelldorf, Germany) were dissolved in deionized water containing the stoichiometric amount of HNO_3 (≥65% Sigma-Aldrich, Schnelldorf, Germany), as if the corresponding $La(NO_3)_3$ and $Mn(NO_3)_2$ salts were used as precursors. Nitrate salts were generated indirectly in the precursor solution by HNO_3 addition because of the high hygroscopic nature of these salts, making the precise amount of cations more controllable with the chosen precursors La_2O_3 and $Mn(CH_3COO)_2$. Citric acid monohydrate (CA, ≥99.0% Sigma-Aldrich, Vienna, Austria) was added according to a molar ratio citric acid/sum of metal cations (CA/M) equal to 1.1 or 1.5. For the synthesis under acidic pH, the solution was directly evaporated overnight at ~120 °C, and a gel was formed, which was then decomposed in an oven at 200–230 °C for 1 h, obtaining a dark solid. For the synthesis under neutral pH, the necessary amount of NH_3 (32%, Sigma-Aldrich, Darmstadt, Germany) was added prior to solvent evaporation as above, and the resulting gel was ignited at 350 °C directly on the hotplate for few minutes, obtaining a dark ash-like solid. In both cases, the obtained solid was grinded and ultimately calcined at 750 °C (ramp 6 °C/min) for 6 h under static air. The same protocol was adopted for the preparation of $La_{0.8}Mn_{0.9}Ni_{0.1}O_3$ and $La_{0.8}Mn_{0.9}Cu_{0.1}O_3$ by dissolving the appropriate amount of $Ni(NO_3)_2{\cdot}6H_2O$ (≥97.0% Sigma-Aldrich, Schnelldorf, Germany) or CuO (≥99.0% Sigma-Aldrich, Tokio, Japan), together with La- and Mn-precursors, in the starting solution. For Ni, the chosen precursor was the nitrate salt and not NiO, since the latter is hardly dissolvable in HNO_3. A synthesis with NiO was attempted, but it resulted in lower crystalline purity of the final perovskite. For doped samples, only the synthesis in acidic pH was carried out, with a CA/M molar ratio of either 1.1 or 1.5. In the Results and Discussion section, the subscript H^+ is used to indicate the synthesis under acidic pH, the subscript NH_3 to indicate the synthesis under neutral pH, and the molar ratio of citric acid/metal cations is indicated by CA1.1 and CA1.5 (see Table 1).

3.2. Characterizations

The decomposition of some selected dried gels was studied by thermogravimetric analysis (TGA) on a LINSESIS 1000 instrument (Linseis Messgeraete GmbH, Selb, Germany). About 10–15 mg of sample, placed in an alumina crucible, were heated under static air from RT to 750 °C at 10 °C/min.

Powder X-ray diffraction (XRD) patterns were acquired with a Bruker D8 Advance diffractometer (Billerica, MA, USA) in Bragg–Brentano geometry, employing a Cu Kα source (λ = 0.154 nm), powered at 40 kV and 40 mA, with steps of 0.02° and a dwell time of 0.35 s/step. Average perovskites' crystallite size was estimated with the Williamson–Hall method by fitting three reflections, i.e., (012), (110) or (104) and (024) (see Figure S1 and Equation (S1)).

N_2 adsorption isotherms were collected at −196 °C with a Micromeritics ASAP2020 Plus instrument (Norcross, GA, USA), in the relative pressure range (p/p^0) of 0.01–1.0, and vice versa; prior to experiments, the samples (~1 g) were outgassed in a vacuum ($p < 1.3$ P_a) at 300 °C for 3 h. Specific surface areas (SSA) were determined according to the Brunauer–Emmett–Teller (BET) model, and pore size distributions according to Barrett–Joyner–Halenda (BJH) model.

H_2 temperature-programmed reduction (TPR) was carried out to investigate the materials' reducibility on a Micromeritics Autochem II 2920 instrument (Norcross, GA, USA). 50 mg of sample were loaded on a U-shaped quartz reactor, above a layer of quartz wool, and heated from RT to 950 °C (ramp 10 °C/min) under a 50 scm^3/min flow of 5% H_2/Ar. The H_2 consumption was monitored with a TCD detector after H_2O absorption by a cold trap.

O_2 temperature-programmed desorption (TPD) was performed on some selected perovskites with the same set-up as for H_2-TPR experiments. About 200 mg of sample were pretreated at 500 °C for 30 min in pure He (50 scm^3/min) and subsequently for 30 min in 5 vol% O_2/He (20 scm^3/min). After cooling down to 40 °C in the same environment, O_2 was allowed to be adsorbed for 30 min. The atmosphere was switched to 30 scm^3/min of He and, after a purging at 40 °C for 15 min to remove physiosorbed oxygen, the sample was finally heated up to 900 °C at 10 °C/min.

Scanning electron microscopy (SEM) images were acquired with a Zeiss SUPRA 40 V P microscope (Zeiss, Oberkochen, Germany), setting the electron acceleration voltage at 5 or 10 kV. Energy-dispersive X-ray analysis (EDX) was coupled with SEM for elemental quantification at 20 kV electron acceleration voltage, probing a large area of sample (rectangle of hundreds of μm on each side); X-ray peaks considered for quantification were O Kα, Mn Kα, La Lα, Ni Kα and Cu Kα.

X-ray photoelectron spectroscopy (XPS) was performed with a Thermo Scientific ESCALAB QXi spectrometer (Waltham, MA, USA), employing a monochromatized Al Kα source (hν = 1486.68 eV) and a charge compensation gun. Survey spectra were acquired at 100 eV pass energy, 0.5 eV/step and 25 ms/step dwell time. Elemental quantification was carried by the integration of La $3d_{5/2}$, Mn 2p, O 1s, Ni 3p and Cu 2p photopeaks (Figure S4), after Shirley-type background subtraction.

3.3. Catalytic Tests

The prepared catalysts were tested for complete oxidation of CH_4 to CO_2 under stoichiometric O_2. A fixed-bed quartz reactor (ID 6 mm) was employed, loading 50 mg of sample between two layers of quartz wool, and a K-type thermocouple was placed in contact with the catalyst bed to monitor its temperature. The reaction mixture was composed of 2 vol% CH_4, 4 vol% O_2, 16 vol% N_2 and He balance, with a total flow rate of 100 scm^3/min (weight hourly space velocity WHSV = 120 L/h/g). The catalytic tests were conducted in the temperature range of 300–800 °C without any pre-treatment of the catalyst, heating up at 2 °C/min. The outlet gas mixture was analyzed by an online GC (Agilent 7890A, Santa Clara, CA, USA) equipped with a TCD detector and two packed columns, MolSieve 13X (60/80 mesh, 1.8 m) and Porapak Q (80/100 mesh, 1.8 m), using He as a carrier gas.

Reaction rates of CH_4 conversion were calculated assuming the mass balance of a plug flow reactor (PFR) and a first-order kinetic with respect to the methane concentration, leading to the following Equations (1) and (2) for the specific rate ($r_{specific}$, normalized by catalyst mass) and intrinsic rate ($r_{intrinsic}$, normalized by catalyst surface area), respectively [36]. X_{CH4} is the methane conversion, m the catalyst mass (g), $F_{CH4,0}$ the inlet molar flow rate of methane (mol/s) and SSA (m^2/g) the catalyst specific surface area as determined from the BET method.

$$r_{specific} = \frac{F_{CH4,0}}{m}(1 - X_{CH4})\ln\frac{1}{1 - X_{CH4}}\ (\mathrm{mol/s/g}) \quad (1)$$

$$r_{intrinsic} = r_{specific}/SSA \left(\mathrm{mol/s/m^2}\right) \quad (2)$$

4. Conclusions

In summary, the A-site-deficient perovskites $La_{0.8}MnO_3$ and $La_{0.8}Mn_{0.9}B_{0.1}O_3$ (B = Ni, Cu) were synthesized through the citrate–nitrate combustion route. The effect of the citric acid/metal cations (CA/M) molar ratio and of the precursor solution's pH on textural, physicochemical and catalytic properties was investigated. It was found that a relatively low CA/M ratio, i.e., 1.1, in conjunction with acidic pH synthesis, produced perovskites featuring a high phase purity, a low crystallite size, a high surface area and mesoporosity and an improved Mn^{4+} reducibility and surface oxygen mobility, thanks to a fast citrate–nitrate decomposition process that likely avoided excessive particle sintering. Instead, both an increase in the CA/M ratio to 1.5 in acidic pH and neutralization by the addition of NH_3 resulted in longer precursor decomposition time and/or higher heat of combustion, increasing the local temperature and producing bigger particles with less porosity, and also decreasing Mn^{4+} reducibility and oxygen mobility. B-site doping with both Ni and Cu cations had a beneficial effect, further improving textural properties and Mn^{4+} reducibility, especially at a CA/M ratio of 1.1. In accordance with the results of physicochemical characterizations, catalytic performances in CH_4 oxidation to CO_2 were much better for samples prepared in acidic pH with a CA/M ratio of 1.1, and the exposed surface area was found to be one of the main factors affecting the catalytic process, in conjunction with the higher Mn^{4+} reducibility and surface oxygen mobility. Cu and Ni doping further improved catalytic activity in the case of a CA/M ratio of 1.5, thanks to improved surface area, reducibility and lattice oxygen mobility, whereas the activity gain was modest and only at low temperatures for samples with a CA/M ratio of 1.1, since in this case, the high temperature activity was mostly dependent on the mobility of lattice oxygen and not improved by B-site doping in contrast to surface oxygen mobility.

Supplementary Materials: The following supporting information can be downloaded at: https://www.mdpi.com/article/10.3390/catal13081177/s1, Figure S1: Extract of XRD pattern with phase matching; Figure S2: BJH pore size distribution; Figure S3: Other SEM micrographs; Figure S4: Representative XPS survey spectra; Equation S1: Williamson–Hall equation; Table S1: EDX and XPS compositions including oxygen content.

Author Contributions: Conceptualization, A.O. and A.G.; methodology, A.G.; validation, A.O., L.R. and J.C.; formal analysis, A.O.; investigation, A.O., L.R. and J.C.; resources, A.G.; visualization: A.O., L.R. and J.C.; writing—original draft preparation, A.O.; writing—review and editing, L.R., J.C. and A.G.; supervision, A.G.; project administration, A.O. and A.G.; funding acquisition, A.G. All authors have read and agreed to the published version of the manuscript.

Funding: This research was supported by European Union HORIZON EUROPE under grant agreement number 101091534 KNOWSKITE-X.

Data Availability Statement: All data are available upon request by contacting the corresponding author: andrea.osti.1@phd.unipd.it.

Acknowledgments: The authors acknowledge the KNOWSKITE-X project for the provision of funding. A special thank goes to Nicola Tiso for TGA measurements.

Conflicts of Interest: The authors declare no conflict of interest. The funders had no role in the design of the study; in the collection, analyses, or interpretation of data; in the writing of the manuscript; or in the decision to publish the results.

References

1. Zhu, J.; Li, H.; Zhong, L.; Xiao, P.; Xu, X.; Yang, X.; Zhao, Z.; Li, J. Perovskite Oxides: Preparation, Characterizations, and Applications in Heterogeneous Catalysis. *ACS Catal.* **2014**, *4*, 2917–2940. [CrossRef]
2. Peña, M.A.; Fierro, J.L.G. Chemical Structures and Performance of Perovskite Oxides. *Chem. Rev.* **2001**, *101*, 1981–2017. [CrossRef] [PubMed]

3. Najjar, H.; Batis, H. Development of Mn-Based Perovskite Materials: Chemical Structure and Applications. *Catal. Rev. Sci. Eng.* **2016**, *58*, 371–438. [CrossRef]
4. Yang, L.; Li, Y.; Sun, Y.; Wang, W.; Shao, Z. Perovskite Oxides in Catalytic Combustion of Volatile Organic Compounds: Recent Advances and Future Prospects. *Energ. Environ. Mater.* **2022**, *5*, 751–776. [CrossRef]
5. Yang, J.; Guo, Y. Nanostructured Perovskite Oxides as Promising Substitutes of Noble Metals Catalysts for Catalytic Combustion of Methane. *Chinese Chem. Lett.* **2018**, *29*, 252–260. [CrossRef]
6. Alifanti, M.; Kirchnerova, J.; Delmon, B.; Klvana, D. Methane and Propane Combustion over Lanthanum Transition-Metal Perovskites: Role of Oxygen Mobility. *Appl. Catal. A Gen.* **2004**, *262*, 167–176. [CrossRef]
7. Spinicci, R.; Delmastro, A.; Ronchetti, S.; Tofanari, A. Catalytic Behaviour of Stoichiometric and Non-Stoichiometric $LaMnO_3$ Perovskite towards Methane Combustion. *Mater. Chem. Phys.* **2002**, *78*, 393–399. [CrossRef]
8. Royer, S.; Alamdari, H.; Duprez, D.; Kaliaguine, S. Oxygen Storage Capacity of $La_{1-x}A'_xBO_3$ Perovskites (with A′=Sr, Ce; B=Co, Mn)—Relation with Catalytic Activity in the CH_4 Oxidation Reaction. *Appl. Catal. B Environ.* **2005**, *58*, 273–288. [CrossRef]
9. Chen, J.; Shen, M.; Wang, X.; Qi, G.; Wang, J.; Li, W. The Influence of Nonstoichiometry on $LaMnO_3$ Perovskite for Catalytic NO Oxidation. *Appl. Catal. B* **2013**, *134–135*, 251–257. [CrossRef]
10. Pinto, D.; Glisenti, A. Pulsed Reactivity on $LaCoO_3$-Based Perovskites: A Comprehensive Approach to Elucidate the CO Oxidation Mechanism and the Effect of Dopants. *Catal. Sci. Technol.* **2019**, *9*, 2749–2757. [CrossRef]
11. Ponce, S.; Peña, M.A.; Fierro, J.L.G. Surface Properties and Catalytic Performance in Methane Combustion of Sr-Substituted Lanthanum Manganites. *Appl. Catal. B Environ.* **2000**, *24*, 193–205. [CrossRef]
12. Marcilly, C.; Courty, P.; Delmon, B. Preparation of Highly Dispersed Mixed Oxides and Oxide Solid Solutions by Pyrolysis of Amorphous Organic Precursors. *J. Am. Ceram. Soc.* **1970**, *53*, 56–57. [CrossRef]
13. Taguchi, H.; Matsu-ura, S.; Nagao, M.; Choso, T.; Tabata, K. Synthesis of LaMnO3 by Firing Gels Using Citric Acid. *J. Solid. State Chem.* **1997**, *129*, 60–65. [CrossRef]
14. Ghiasi, E.; Malekzadeh, A.; Ghiasi, M. Moderate Concentration of Citric Acid for the Formation of $LaMnO_3$ and $LaCoO_3$ Nano-Perovskites. *J. Rare Earths* **2013**, *31*, 997–1002. [CrossRef]
15. Sihaib, Z.; Puleo, F.; Pantaleo, G.; La Parola, V.; Valverde, J.L.; Gil, S.; Liotta, L.F.; Fendler, A.G. The Effect of Citric Acid Concentration on the Properties of $LaMnO_3$ as a Catalyst for Hydrocarbon Oxidation. *Catalysts* **2019**, *9*, 226. [CrossRef]
16. Li, Y.; Xue, L.; Fan, L.; Yan, Y. The Effect of Citric Acid to Metal Nitrates Molar Ratio on Sol-Gel Combustion Synthesis of Nanocrystalline $LaMnO_3$ Powders. *J. Alloys Compd.* **2009**, *478*, 493–497. [CrossRef]
17. Nakamura, T.; Misono, M.; Yoneda, Y. Catalytic Properties of Perovskite-Type Mixed Oxides, $La_{1-x}Sr_xCoO_3$. *Bull. Chem. Soc. Jpn.* **1982**, *55*, 394–399. [CrossRef]
18. Schön, A.; Dujardin, C.; Dacquin, J.-P.; Granger, P. Enhancing Catalytic Activity of Perovskite-Based Catalysts in Three-Way Catalysis by Surface Composition Optimisation. *Catal. Today* **2015**, *258*, 543–548. [CrossRef]
19. Esmaeilnejad-Ahranjani, P.; Khodadadi, A.; Ziaei-Azad, H.; Mortazavi, Y. Effects of Excess Manganese in Lanthanum Manganite Perovskite on Lowering Oxidation Light-off Temperature for Automotive Exhaust Gas Pollutants. *Chem. Eng. J.* **2011**, *169*, 282–289. [CrossRef]
20. Zhang, C.; Zeng, K.; Wang, C.; Liu, X.; Wu, G.; Wang, Z.; Wang, D. $LaMnO_3$ Perovskites via a Facile Nickel Substitution Strategy for Boosting Propane Combustion Performance. *Ceram. Int.* **2020**, *46*, 6652–6662. [CrossRef]
21. Esmaeilnejad-Ahranjani, P.; Khodadadi, A.A.; Mortazavi, Y. Self-Regenerative Function of Cu in $LaMnCu_{0.1}O_3$ Catalyst: Towards Noble Metal-Free Intelligent Perovskites for Automotive Exhaust Gas Treatment. *Appl. Catal. A Gen.* **2020**, *602*, 117702. [CrossRef]
22. Shannon, R.D. Revised Effective Ionic Radii and Systematic Studies of Interatomie Distances in Halides and Chaleogenides. *Acta Cryst.* **1976**, *32*, 751–767. [CrossRef]
23. Gholizadeh, A. X-Ray Peak Broadening Analysis in $LaMnO_{3+\delta}$ Nano-Particles with Rhombohedral Crystal Structure. *J. Adv. Mater. Process.* **2015**, *3*, 71–83.
24. Frozandeh-Mehr, E.; Malekzadeh, A.; Ghiasi, M.; Gholizadeh, A.; Mortazavi, Y.; Khodadadi, A. Effect of Partial Substitution of Lanthanum by Strontium or Bismuth on Structural Features of the Lanthanum Manganite Nanoparticles as a Catalyst for Carbon Monoxide Oxidation. *Catal. Commun.* **2012**, *28*, 32–37. [CrossRef]
25. Thommes, M.; Kaneko, K.; Neimark, A.V.; Olivier, J.P.; Rodriguez-Reinoso, F.; Rouquerol, J.; Sing, K.S.W. Physisorption of Gases, with Special Reference to the Evaluation of Surface Area and Pore Size Distribution (IUPAC Technical Report). *Pure Appl. Chem.* **2015**, *87*, 1051–1069. [CrossRef]
26. Wu, J.; Zheng, Y.; Dacquin, J.P.; Djelal, N.; Cordier, C.; Dujardin, C.; Granger, P. Impact of Dual Calcium and Manganese Substitution of La-Deficient Perovskites on Structural and Related Catalytic Properties: Future Opportunities in next Three-Way-Catalyst Generation? *Appl. Catal. A Gen.* **2021**, *619*, 118137. [CrossRef]
27. Feick, G.; Hainer, R.M. On the Thermal Decomposition of Ammonium Nitrate. Steady-State Reaction Temperatures and Reaction Rate. *J. Am. Chem. Soc.* **1954**, *76*, 5860–5863. [CrossRef]
28. Brusamarello, E.; Blonda, C.; Salazar-Castro, C.; Pascui, A.E.; Canu, P.; Glisenti, A. Industrially Produced Fe- And Mn-Based Perovskites: Effect of Synthesis on Reactivity in Three-Way Catalysis: Part 1. *ACS Omega* **2021**, *6*, 24325–24337. [CrossRef]
29. Brusamarello, E.; Blonda, C.; Salazar-Castro, C.; Canu, P.; Glisenti, A. Industrially Produced Fe- And Mn-Based Perovskites: Effect of Synthesis on Reactivity in Three-Way Catalysis: Part 2. *ACS Omega* **2021**, *6*, 24316–24324. [CrossRef]

30. Giordano, F.; Trovarelli, A.; De Leitenburg, C.; Giona, M. A Model for the Temperature-Programmed Reduction of Low and High Surface Area Ceria. *J. Catal.* **2000**, *193*, 273–282. [CrossRef]
31. Wei, T.; Jia, L.; Zheng, H.; Chi, B.; Pu, J.; Li, J. LaMnO3-Based Perovskite with in-Situ Exsolved Ni Nanoparticles: A Highly Active, Performance Stable and Coking Resistant Catalyst for CO_2 Dry Reforming of CH_4. *Appl. Catal. A Gen.* **2018**, *564*, 199–207. [CrossRef]
32. Patcas, F.; Buciuman, F.C.; Zsako, J. Oxygen Non-Stoichiometry and Reducibility of B-Site Substituted Lanthanum Manganites. *Termochimica Acta* **2000**, *360*, 71–76. [CrossRef]
33. Huang, C.; Shan, W.; Lian, Z.; Zhang, Y.; He, H. Recent Advances in Three-Way Catalysts of Natural Gas Vehicles. *Catal. Sci. Technol.* **2020**, *10*, 6407–6419. [CrossRef]
34. Mars, P.; van Krevelen, D.W. Oxidations Carried out by Means of Vanadium Oxide Catalysts. *Chem. Eng. Sci.* **1954**, *3*, 41–59. [CrossRef]
35. Hammami, R.; Aïssa, S.B.; Batis, H. Effects of Thermal Treatment on Physico-Chemical and Catalytic Properties of Lanthanum Manganite $LaMnO_{3+y}$. *Appl. Catal. A Gen.* **2009**, *353*, 145–153. [CrossRef]
36. Wu, J.; Dacquin, J.P.; Djelal, N.; Cordier, C.; Dujardin, C.; Granger, P. Calcium and Copper Substitution in Stoichiometric and La-Deficient $LaFeO_3$ Compositions: A Starting Point in next Generation of Three-Way-Catalysts for Gasoline Engines. *Appl. Catal. B* **2021**, *282*, 119621. [CrossRef]